

CARBON-RICH MOLECULAR CHAINS IN PROTOPLANETARY AND PLANETARY ATMOSPHERES: QUANTUM MECHANISMS AND ELECTRON ATTACHMENT RATES FOR ANION FORMATION

F. CARELLI¹, M. SATTÀ², T. GRASSI¹, AND F. A. GIANTURCO^{1,3}

¹ Department of Chemistry and CNISM, The University of Rome “Sapienza,” Piazzale Aldo Moro 5, 00185 Rome, Italy; francesco.gianturco@uniroma1.it

² CNR-ISMN and University of Rome “Sapienza,” Piazzale Aldo Moro 5, 00185 Rome, Italy

Received 2013 May 3; accepted 2013 July 15; published 2013 August 20

ABSTRACT

The elementary mechanisms through which molecular polyynes could form stable negative ions after interacting with free electrons in planetary atmospheres (e.g., Titan’s) are analyzed using quantum scattering calculations and quantum structure methods. The case of radical species and of nonpolar partners are analyzed via specific examples for both the C_nH and HC_nH series, with n values from 4 to 12. We show that attachment processes to polar radicals are dominating the anionic production and that the mediating role of dipolar scattering states is crucial to their formation. The corresponding attachment rates are presented as calculated upper limits to their likely values and are obtained down to the low temperatures of interest. The effects of the computed rates, when used in simple evolutionary models, are also investigated and presented in detail.

Key words: astrochemistry – evolution – ISM: clouds – ISM: molecules – molecular processes

Online-only material: color figures

1. INTRODUCTION

The likely existence of molecular species with negative charges (anionic molecules) in the interstellar medium (ISM) was put forward a long time ago by several groups (Dalgarno & McCray 1973; Sarre 1980; Herbst 1981). These authors also suggested via simple models that carbon chains and hydrocarbon radicals would have large electron affinities (EAs) and would lead to efficient electron attachment rates, chiefly by radiative stabilization (RS) of molecular anions with more than four to five atoms.

Experimental proof of these hypotheses was provided later by laboratory data concerning the rotational spectrum of C_6H^- (McCarthy et al. 2006), which was seen in the astronomical spectra of Kawaguchi et al. (1995). These data established the presence of C_6H^- in the envelope of the carbon-rich IRC+10216 star. The same species was further determined by McCarthy et al. (2006) in the Taurus Molecular Cloud 1 cyanopolyne peak (TMC-1(CP)).

Laboratory spectra of other anionic molecules like C_4H^- , C_8H^- , and C_3N^- have also been determined in the laboratory (e.g., see Thaddeus et al. 2008) and subsequently observed by Cernicharo et al. (2007, C_4H^-), Remijan et al. (2007, C_8H^-), and Thaddeus et al. (2008, C_3N^-) in the envelope of IRC+10216 and also in the TMC-1 (C_8H^- by Brünken et al. 2007).

Several molecular ions were surveyed by Gupta et al. (2007), who detected C_6H^- in two further sources: the pre-stellar cloud L1544 and the protostellar object L1521F. Cernicharo et al. (2008) attributed a series of rotational lines observed in the envelope of IRC+10216 to another molecular anion: C_5N^- .

Since such anionic species have turned out to be present under different conditions and in significant abundances (i.e., the measured column density of C_6H^- in the TMC-1(CP) was found to be 10^{11} cm^{-2} ; see McCarthy et al. 2006), it is now realistic to surmise that these species play a more significant role in the chemistry of astrophysical environments than previously expected. Hence, it becomes necessary to investigate more

specifically what would be the nanoscopic mechanism that could be invoked to explain their initial formation and their final stabilization and/or fragmentation into smaller anionic species.

The general dynamics of free electrons interacting with various polyynes has been recently studied from the theoretical/computational side in our group, where we have investigated the resonant attachment of low-energy electrons to NCCN (Sebastianelli et al. 2012) and the transient metastable anions of NC_4N (Sebastianelli & Gianturco 2010). We have also studied the possible fragmentation pathways of HC_3N and HC_5N negative ions (Sebastianelli & Gianturco 2012). A more recent study on anionic formation mechanisms of HC_4H has also been carried out by some of the above authors (Baccarelli et al. 2013).

Since it is becoming increasingly more important at the molecular level to clarify the physical mechanisms for the formation of stable negative ions of carbon-rich molecular chains and to generate reliable estimates for the attachment rates of electrons to such species (Walsh et al. 2009), the present study is an attempt at combining the methods of quantum molecular dynamics for the processes that preside over electron attachment to the neutral partners of the polyynes described here. We generate actual attachment rate values at the temperatures of interest through a simplified treatment of the electron attachment reactions. These attachment rate values will be further tested in terms of their effects on evolutionary models and existing chemical networks will be employed to verify the actual influence of the values of the rates that are produced in the present work.

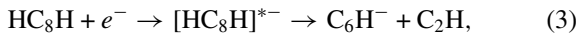
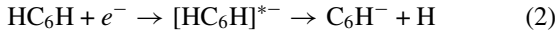
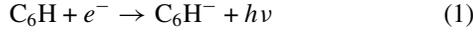
This paper is organized as follows: the next section, Section 2, discusses some of the properties of the molecules of this study that are relevant to the attachment reactions with electrons and the chemical evolutions that could lead to stabilizing molecular anions. Section 3 presents our computational methods for the quantum dynamics of electron collisions with polyynes. The results of electron collisions are given in Section 4 while Section 5 discusses the calculations of the attachment rates. The influence of the attachment rates on the evolutionary models

³ Corresponding author.

is reported in Section 6, while our conclusions are given in Section 7.

2. POLAR AND NONPOLAR MOLECULAR PARTNERS

The observational findings, briefly discussed in the previous section, point to the presence of anionic molecules chiefly derived from radical species that are C-rich, with either H or N as one terminating atom; in the case of hydrogen-containing species, the C_6H^- component was found to be among the most abundant. For this species in particular, one can envision the following possibilities for actual formation:



where the reactions (1)–(3) qualitatively sketch the direct attachment process (1) suggested by Harada & Herbst (2008), the dehydrogenation process after resonant attachment to a nonradical partner (2), as found in laboratory experiments on a range of polyynes (e.g., Graupner et al. 2008) and the fragmentation path following the primary electron attachment (Walsh et al. 2009) to a larger polyyne partner. The above paths indicate the various possibilities of (1) direct stabilization of a bound anionic species, (2) the dissociative attachment (DA) stabilization of the anionic species by H losses, and (3) stabilization of smaller anionic species by DA via C–C bond breaking leading to smaller stable anions. The last mechanism is particularly relevant for discussing the stabilizing paths involving larger polyynes that can lead to the appearance of the observed smaller components, e.g., C_4H^- and C_6H^- (Harada & Herbst 2008).

Within the above context, it is important to note two crucial properties of the class of molecules we are considering here: the values of their dipole moments and their EAs. In the first instance, the radical species C_nH that we are considering all exhibit strong permanent dipole moments, with values much larger than the critical dipole moment responsible for binding an extra electron to the relevant species (e.g., Simons 2008). Such a feature is often considered indicative of the fact that the molecule in question can have a dipole bound state (DBS) of its anion that is now more stable than its neutral partner by a very small energy value and is usually localized well outside the molecular space occupied by valence electrons (e.g., Desfrancois 1995; Carles et al. 2000). We will further discuss this aspect of the attachment path in the following sections, where we will show how a quantum scattering study of low-energy free electrons interacting with polyyne radicals can indeed also lead to dipolar states in the continuum for the metastable anions. Here, it is important to mention that all radical species under consideration have sufficiently large dipole moments to verify the condition for DBS formation, thus indicating the real possibility of forming bound anionic states with very small EAs with respect to the ground-state valence anions that exhibit the large EAs reported in Table 1.

It is also of interest to see how similar dipole-driven scattering configurations (which could lead to DBS formation) could also be obtained for nonpolar linear species by vibrational excitations of the latter through a variety of mechanisms already present in the interstellar environment (e.g., photon excitation,

Table 1
Linear Carbon Chains Studied in the Present Work

	μ (D) ^a	EA (eV) ^b	α_0 (a_0^3) ^c
HC ₄	0.866	3.42	53.70
HC ₆	5.069	3.64	95.89
HC ₈	5.741	4.53	145.00
HC ₁₀	6.280	4.72	183.18
HC ₄ H	0.0	−0.641	33.20
HC ₆ H	0.0	0.221	88.53
HC ₈ H	0.0	0.891	132.65
HC ₁₀ H	0.0	1.380	198.01
HC ₁₂ H	0.0	1.790	276.66

Notes. All the calculations involving the dipole were performed at the level (RO)HF/6-311++G(3df,3pd); the EA and the polarizabilities were instead obtained at the (RO)B3LYP/6-311++G(3df,3pd) level. See the main text for further details.

^a Computed dipole, in Debye.

^b EA, in eV.

^c Static polarizability α_0 , in cubic Bohrs.

electron-impact energy transfer, resonant electron attachment, and others).

We have collected in Table 1 significant data about a set of polyynes and polyyne radicals that are relevant for the present study, i.e., radicals with n values from $n = 4$ to $n = 12$. The following features will be important in the present discussion on anion formation.

1. The radical species show large permanent dipole moments that are increasingly larger than the critical value (μ_{cr}) of 1.625 D mentioned in the relevant literature (Garret 1982; Fermi & Teller 1947), thus indicating that such species would be able to form electronically excited anions with positive EA values in the meV range (the DBS configurations discussed above). Because of its permanent dipole value, however, the HC₄ molecule is in principle not expected to form such a state. In our present modeling, this result could be linked to its observationally reduced existence as a stable anion; in this respect, it is worth mentioning that the above molecule has another specific property of its first excited electronic state of $^2\Pi$ symmetry: it has been found to lie very close to the ground state (around 100 cm^{-1}) and to present a much larger permanent dipole moment (>4 Debye; McCarthy et al. 1995). Thus, the molecule can indeed form a DBS anion in its excited electronic state, although it would not play a significant role in increasing the abundance of that species with respect to the longer chains because of the environmental conditions.
2. The same radical species also exhibit valence anionic configurations with EA values that are much higher (in the 3–5 eV range) and therefore would get radiatively stabilized with much larger energy emission or could undergo internal vibrational redistribution (IVR) processes likely to cause further bond breaking that will remove their contribution from the observed column density in ISM regions.
3. The nonpolar polyynes, on the other hand, show much smaller EA values, all around or below the 1 eV threshold. These values indicate that anionic formation from resonant states by RS could be a realistic option, as we will further show and analyze in the following sections.
4. The spherical polarizabilities are also interesting indicators of the species' capabilities to interact with threshold electrons as free agents in the ISM and in the outer regions of

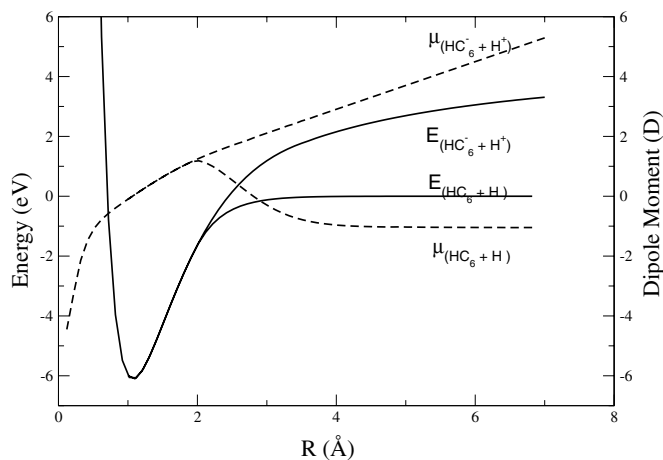


Figure 1. Computed potential curve for the asymmetric stretching of one H atom in HC_6H . The scale on the left reports energy values in eV, while the scale on the right shows the dipolar values. The thinner solid curve refers to the ionic break-up of the system.

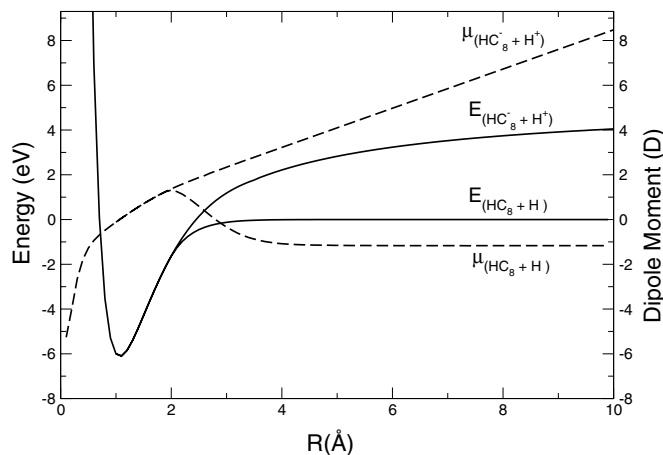


Figure 2. Same as in Figure 1, but for the carbon bearing linear chain with $n = 8$. See the main text for further details.

the photodissociation region environments: the polarizability values (α_0), in fact, increase along the series and play an important role in the following discussion on low-energy resonant states of metastable polyynes anions.

In conclusion, even before starting to carry out our calculations, the properties of the present polyynes already suggest the following.

1. The radical species could form stable anionic molecules through the formation of dipolar states in the continuum (that we call dipole scattering states (DSSs)), followed by relaxation into discretized bound anions as DBSS.
2. The nonpolar polyynes could form metastable resonances at low energies and then decay into bound anions with smaller EAs than their radical counterparts. Hence, these nonpolar polyynes are more likely to form such anions without dissociative paths from the initial state.
3. Coupling effects leading to vibrational excitation of nonpolar polyynes by interactions with the low-energy resonant electrons is also a distinct possibility, one now leading to the presence of an induced dipole in the metastable species that we shall also discuss below.

To provide some computational evidence for the possible paths to DSS formation in distorted nonpolar polyynes, we

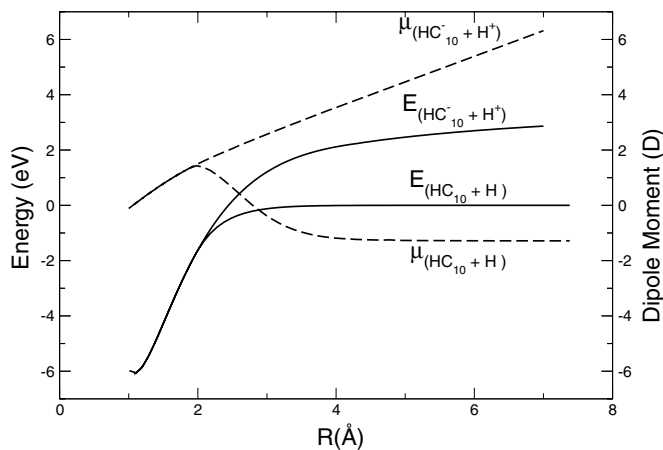


Figure 3. Same as in Figure 1 but for the linear chain with $n = 10$ in HC_nH . See the text for further details.

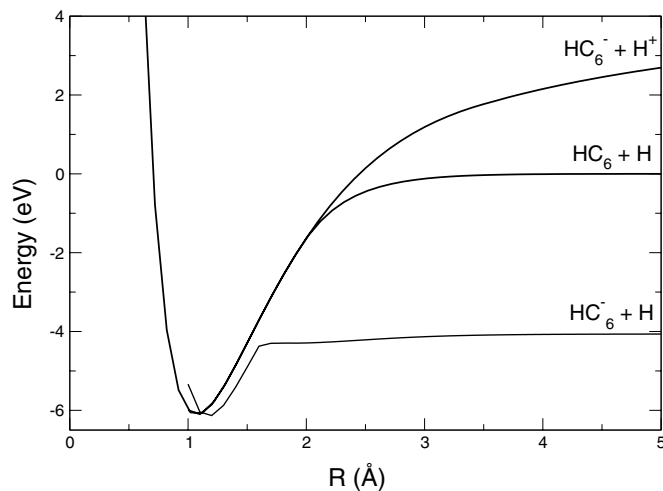


Figure 4. Computed potential curves for the cases of ionic (upper curve) and radical (central curve) break-up, in comparison with the formation of a stable anionic species and an H atom (bottom curve).

present in Figures 1–4 the quantum chemical calculations for the asymmetric stretching occurring as one of the terminal H atoms is moved away from the equilibrium positions. It is worth noting that the following calculations, reported by Figures 1–4, are intended to show at a semiquantitative level the feasibility of the process we will discuss later more quantitatively. Thus, the choice of basis set expansions of medium quality is dictated by the intended role of such calculations in the present study.

The calculations were carried by using an extended basis set of 6-31++G** Gaussian-type orbitals (GTOs) including correlation effects at the DFT level with B3LYP.

It is interesting to note at the beginning that the radical path to separation produces a lower barrier from the initial bound states but the corresponding dipole moment tends to vanish as R increases, the latter being the stretching C–H coordinate defined before. On the other hand, the cation–anion (polar) break-up shows an increasing barrier to that separation, while, however, the dipole value steadily increases as R increases; the final formation of $\text{C}_6\text{H}^- + \text{H}^+$ is indeed the cause for that increase. It indicates that the critical value of the dipole is reached only along the ionic curve and, in the present calculations, occurs around 3 Å of bond stretching for the terminal C–H.

A similar behavior is shown in Figures 2 and 3 for the longer polyynes with $n = 8$ and $n = 10$. The calculations were carried

out at the same level of basis set choice and correlation inclusion as in Figure 1.

The general behavior of the present systems reported by Figures 2 and 3 is indeed very similar, although dipole moments around the critical value of 1.625 D are reached at longer distances for HC₈H (~2 Å) than for HC₁₀H (<2 Å). In both systems, however, the ionic break-up path is the one that supports dipole moment values beyond μ_{cr} .

It is also interesting to note that, in ionic break-up, all systems localize their negative charge on the larger radicals since C_nH⁻ is always formed, while the residual is always given by the H⁺-end of the stretching bond. If one now considers the presence of an environmental electron, it is reasonable to expect that the latter will preferentially localize itself on the cationic region so that a neutral H atom would be produced, attached by polarization forces to the HC_n⁻ moiety and with a marked energy gain because of the large ionization potential (IP) of the H atom (13.67 eV). Hence, in spite of the energy increase along the ionic separation path, the system will be finally stabilized by the H-atom formation.

This type of behavior is presented, as an example, for the case of HC₆H. We discussed this case previously but now compared with the relative position of an anionic moiety attached to an H atom; see Figure 4.

In spite of the simplicity of these one-dimensional calculations meant to provide at least an initial proof of point for the effects discussed here, we see from the PECs shown in Figure 4 that the attachment of an extra electron produces a marked lowering of the asymptotic energy for the species bound by induction forces, the HC₆⁻ + H system. The energy difference in the asymptotic region with the HC₆ + H neutral radical upper asymptotes yields correctly a vertical EA of the radical of about 4 eV, i.e., close to the estimate reported in Table 1 for this molecule.

In other words, what the above calculations show is the possibility that both the radical polynes and the nonpolar closed-shell counterparts could undergo stabilization as anionic moieties in interaction with free electrons at low energies. How this effect could be described by quantum scattering models is discussed in detail in the following sections.

3. QUANTUM COLLISIONS WITH FREE ELECTRONS: AN OUTLINE OF THE METHOD

The theoretical/computational method we use in the present work has been described in full detail many times before (Lucchese & Gianturco 1996), so that we only provide a brief outline here.

In the framework of the Born–Oppenheimer approximation, the electron–molecule collision is performed following the time-independent approach. The total wave function describing the neutral molecular target plus the incoming electron is represented as an antisymmetrized linear superposition of one-electron wave functions, which parameterically depend on the nuclei positions and where the bound molecular electrons are described at the Hartree–Fock (HF) level.

Our computational approach to the electron–molecule scattering event rests on the single-center-expansion (Lucchese & Gianturco 1996), according to which all the one-electron orbitals involved (including both the target bound orbitals and the colliding electron wave function in the continuum), as well as all the interaction potentials, are expanded as linear combinations

of symmetry-adapted spherical harmonics:

$$\phi_i^{p\mu}(r, \theta, \varphi) = \frac{1}{r} \sum_{\ell h} u_{\ell h}^{p\mu}(r) X_{\ell h}^{p\mu}(\theta, \varphi), \quad (4)$$

where $X_{\ell h}^{p\mu}(\theta, \varphi)$ indicates the linear combinations of spherical harmonics $Y_{\ell}^{p\mu}$ and the $|p\mu\rangle$ labels refer to the specific irreducible representation indices (Lucchese & Gianturco 1996).

We go beyond the static-exchange approximation, according to which the target molecule is described at a sufficiently adequate level by its ground-state Slater determinant, by additionally introducing both the correlation and the polarization terms that take into consideration the molecular response to the incoming electron at short and large distances, respectively. That adjunctive part of the electron–molecule interaction has been modeled by considering:

$$V_{cp}(r) = \begin{cases} V_{corr}(r) & \text{for } r \leq r_{match} \\ V_{pol}(r) & \text{for } r > r_{match} \end{cases}, \quad (5)$$

where we use the Perdew–Zunger model for the correlation (Perdew & Zunger 1981). The long-range polarization term is indeed introduced as a function of the molecular polarizability tensor and is connected with the previous term by an appropriate matching function centered on r_{match} .

According to the previous assumptions, the short-range potential should still not only be energy-dependent, but also non-local. It therefore follows that, in order to have only an overall local interaction potential, we also introduce the so-called free electron gas exchange potential proposed by Hara (1967; HFEGE):

$$V_{HFEGE}(\mathbf{r}) = -\frac{2}{\pi} K_F(\mathbf{r}) \Lambda(\eta) \\ \Lambda(\eta) = \left[\frac{1}{2} + \frac{1-\eta^2}{4\eta} \ln \left(\frac{1+\eta}{1-\eta} \right) \right], \quad (6)$$

where K_F is the Fermi momentum and η is the ionization potential for the neutral molecular target. In this conjunction, we find it important to emphasize that the latter hypothesis was tested many times before; it provides a realistic description of the exchange forces in a great variety of molecular systems.

By introducing all of the above assumptions, the scattering equation can therefore be recast in a homogeneous form:

$$\left[-\frac{1}{2} \nabla^2 - \frac{1}{2} k^2 + V(\mathbf{r}) \right] F(\mathbf{r}) = 0, \quad (7)$$

which constitutes our static-model-exchange-correlation-polarization approximation, used throughout the present study. The potential $V(\mathbf{r})$ is the sum of the three local potentials $V(\mathbf{r}) = V_{st}(\mathbf{r}) + V_{cp}(\mathbf{r}) + V_{HFEGE}(\mathbf{r})$, where the last term describes the Columbian static interaction that takes place between the colliding electron and the neutral molecule’s nuclei and bound electrons. Eventually, integration over the angular variables (θ, φ) of Equation (7) yields the radial coupled differential equations that we numerically solve by propagating the scattered electron radial wave function $u_{\ell h}^{p\mu}(r)$ using standard real scattering boundary conditions (Taylor 1972):

$$\left[\frac{d^2}{dr^2} - \frac{\ell(\ell+1)}{r^2} + k^2 \right] u_{\ell h}^{p\mu}(r) \\ = 2 \sum_{\ell' h'} \int dr' V_{\ell h, \ell' h'}^{p\mu}(r) u_{\ell' h'}^{p\mu}(r), \quad (8)$$

where the potential coupling elements are given by

$$\begin{aligned} V_{lh,l'h'}^{p\mu}(r) &= \langle \chi_{lh}^{p\mu}(\hat{r}) | V(\mathbf{r}) | \chi_{l'h'}^{p\mu}(\hat{r}) \rangle \\ &= \int d\hat{r} \chi_{lh}^{p\mu}(\hat{r}) V(\mathbf{r}) \chi_{l'h'}^{p\mu}(\hat{r}). \end{aligned} \quad (9)$$

One of the electron attachment processes we are looking at in the present study is one where the excess energy carried by the colliding electron, when temporarily captured by the molecular potential in a metastable state via shape resonance, could be gathered into the internal molecular energy (i.e., the molecular bonds could either partially or totally receive that energy amount). In such a case, it therefore makes sense to presume the formation of new anionic species that could be born via dissociative electron attachment (DEA); we will show that the initial formation of long-lived metastable anions with the dipole-driven threshold electrons (DSS states) plays a role as the preferential gateway for the overall process. In connection with the above observation, we therefore surmise that within the highly diluted ISM environment, where the time between two consecutive collisions involving the same target typically far exceeds the relaxation time, such transient species could also be easily stabilized by radiatively dissipating the extra energy (RS), thus evolving into an excited anionic DBS.

Furthermore, we know that radiative attachment rates have already been assessed for linear molecules like C_3N , C_n , and HC_n by Harada & Herbst (2008) under the limited assumption that only s-wave electrons with energies close to zero could provide efficient attachment. On the other hand, however, the resonances located at higher energies constitute in principle other possible attachment channels for which the extra energy brought by the resonant electron still needs to be dissipated within the molecular network due to the possible coupling between the metastable electron and the molecular vibrational modes. Hence, as will be discussed in detail in the next sections, we are suggesting here the likely fragmentation path taking place along a specific bond, the terminal C–H bond, as that one responsible of the overall stabilization of a molecular polar anion that is in turn begun by the disrapture of that bond during the metastable complex lifetime. In this sense, it stands to reason that the radiative dissipative stabilization path may also represent a physically realistic possibility: the energy amount that once again still needs to be dissipated by the excited anionic structure, in fact, is relatively small and consequently the RS process can indeed occur before the competitive autodetachment (AD) channel takes place.

The above picture of the dynamical stabilization of closed-shell polyynes anions has been outlined in the previous section, while a more general analysis of attachment rates has been presented by our group for a larger variety of polyynes (Carelli et al. 2013). In the present study, the above computational machinery will be extended to model attachment to radical polar systems with the view that the latter can undergo direct stabilization via DSS formation as outlined in the previous section and as detailed below. Hence, the present calculations will focus on the formation of dipole states in the continuum for polar targets of linear, carbon-rich chains, either directly by electron scattering to radicals or mediated by initial low-energy resonances of the nonpolar systems, which then undergo IVR coupling leading to polar intermediates and to H-atom detachment.

4. RESONANT AND DIPOLAR SCATTERING STATES

4.1. Resonances for Nonpolar Polyynes

As we discussed in the previous sections, the presence of metastable anionic states in the continuum is an important feature for establishing the role of gateway states of the systems that could efficiently evolve into either bound valence anions of that molecule or decay via DEA mechanisms into smaller, stable anionic partners.

We have already seen that the HC_4H molecule (Baccarelli et al. 2013) shows a fairly narrow resonance around 2 eV that unequivocally exhibited π^* features and that could lead to DEA processes following the simple path $[HC_4H]^{-*} \rightarrow C_4H^- + H$ that we know from quantum chemical calculations to be an exothermic path due to its large EA (Table 1). We therefore extended the analysis to the longer members of the polyynes series of closed-shell, nonpolar molecules HC_nH with n ranging from 6 to 12. The calculations were carried out following the procedure described in the previous sections. We employed a multipolar expansion of the interaction potential up to $L_{\max} = 140$, while the scattered electron partial wave expansion was extended up to $l_{\max} = 70$. The internal box within which the full potential was included in the scattering calculation was extended up to $R_{\max} = 50$. The polarizability values, collected in Table 1, were obtained from ab initio quantum calculations at the level B3LYP/6-311++G(3df,3pd) (Frisch 2009).

Figures 5 and 6 report the lowest resonant states for each of the systems of the series discussed in the present work. One must combine these data with the results for HC_4H (Baccarelli et al. 2013), which show a narrow resonance around 2.0 eV, in agreement with experiments (Allan et al. 2011). No other shapes or Feshbach resonances up to about 6 eV are observed.

In Figure 5, the top panels show the lowest resonant state for HC_6H , a ${}^2\Pi_g$ state located at 1.24 eV with a fairly long lifetime. The lower panels show the results for the HC_8H system: the resonance has now moved down in energy and has become narrower, as clearly shown by the behavior of the eigenphase sums reported in the panel on the left.

The next larger members of the polyynes series are presented in Figure 6. The data in the top panels refer to the $HC_{10}H$ case and clearly confirm the trend observed for the previous terms of the series: the lowest ${}^2\Pi_g$ resonance moves down further in energy and becomes even more long lived. The data thus indicate that these resonant states are located close to the threshold as the series moves to longer carbon-rich chains and their longer lifetimes become increasingly more competitive against the AD of the metastable electron. It therefore stands to reason that such temporary anionic compounds could either decay directly into stable anions for each of the species either leading to the valence anions in their ground states (given the fairly small EAs reported in Table 1) or could undergo DEA by de-hydrogenation following asymmetric stretching deformations leading to polar intermediates as shown by the structure calculations of Section 2. This latter mechanism would therefore add the presence of C_nH^- species from the possible existence of HC_nH precursors, which would have been formed in the ISM through other mechanisms not to be further discussed in the present study.

The data in the bottom panels of Figure 6 refer to the next term in the series, $HC_{12}H$: we see here, as could have been expected, a fairly dramatic change in the resonance features. They move up in energy since they are now located at 1.7 eV, and they become much broader than the previous term in the series. Furthermore,

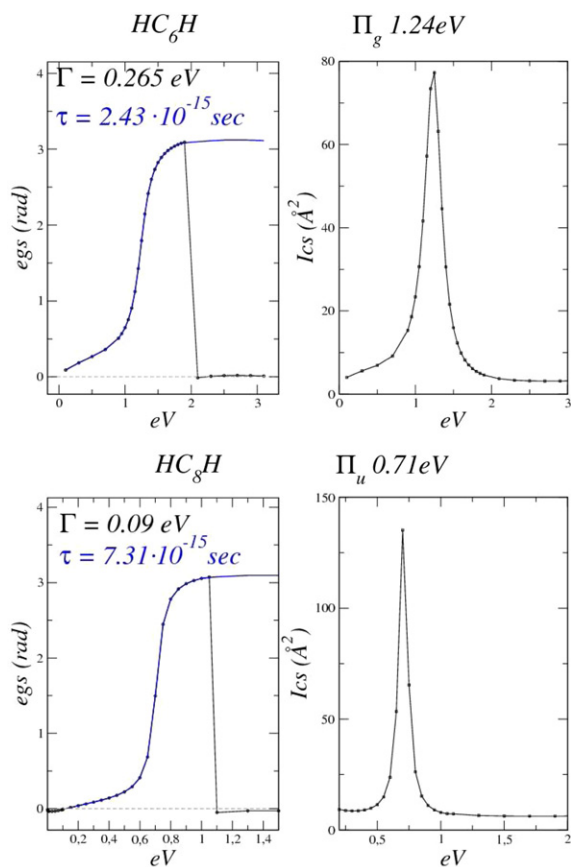


Figure 5. Computed π^* resonances for the HC_6H and HC_8H polyynes. In the first column, the behavior of the eigenphase sums are shown. In the second column, the partial integral cross sections around the resonance features are shown. (A color version of this figure is available in the online journal.)

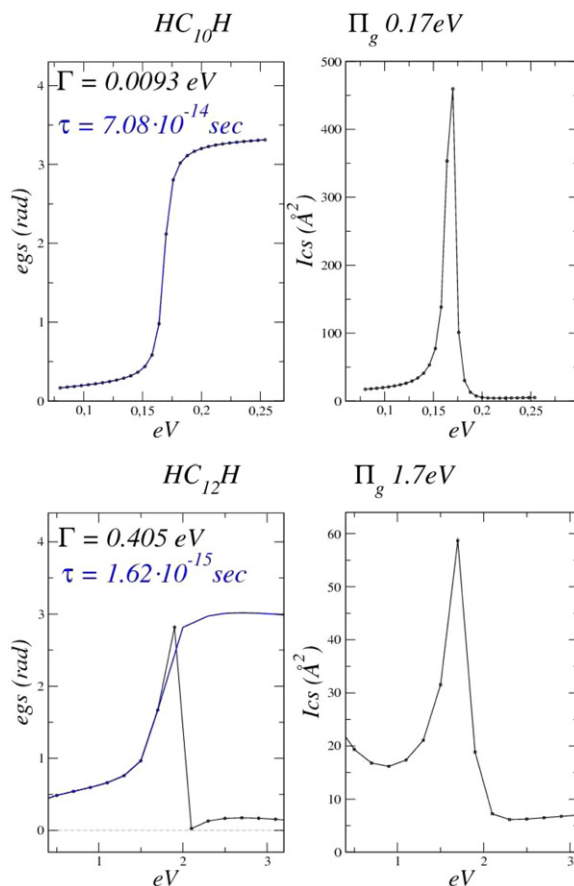


Figure 6. Same data as in Figure 5 but for the larger polyynes HC_{10}H and HC_{12}H . See the main text for further details.

(A color version of this figure is available in the online journal.)

Table 2
Computed Features of the π^* -shape Resonances Detected for the Polyynes Series within the Energy Range 0 eV to about 6 eV

	E (eV)	Γ (eV)	τ (s)	Symm
HC_6H	1.24	0.265	2.43×10^{-15}	$(^2\Pi_g)$
HC_8H	0.71	0.090	7.31×10^{-15}	$(^2\Pi_u)$
HC_8H	3.70	1.030	6.38×10^{-16}	$(^2\Pi_g)$
HC_{10}H	0.17	0.0093	7.08×10^{-14}	$(^2\Pi_g)$
HC_{10}H	2.70	0.430	1.53×10^{-15}	$(^2\Pi_u)$
HC_{12}H	1.72	0.405	1.62×10^{-15}	$(^2\Pi_g)$
HC_{12}H	4.15	0.762	8.67×10^{-16}	$(^2\Pi_u)$

Note. E = energy location of resonance (in eV); Γ = linewidth of resonance (in eV); τ = resonance lifetime (in sec.); Symm = point-group symmetry of the metastable state.

they do not follow the alternance between $^2\Pi_u$ resonance (as in HC_4H) to the $^2\Pi_g$ (HC_6H), to the $^2\Pi_u$ again (HC_8H), and to $^2\Pi_g$ (HC_{10}H). Clearly, the expected narrower resonance closer to the threshold and of the $^2\Pi_g$ character has become a bound state for the HC_{12}H system and the next higher resonance in this molecule has now come down in energy, thus becoming the lowest visible resonance.

The calculations reported in Table 2 indeed confirm such a behavior and show the appearance of a second resonance at higher energies and with different nodal structure for the terms in the series with more carbon atoms in the chains. The second resonances are in fact present from HC_8H to HC_{12}H and confirm their gradual shifting to lower energies and their

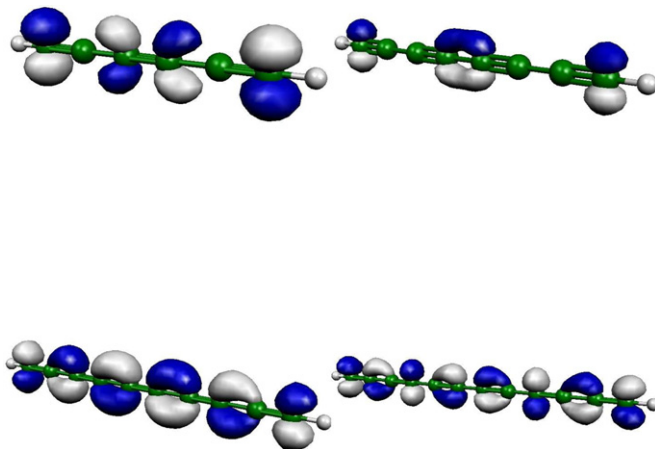


Figure 7. Computed scattering wave functions (real part) at the energies of the lowest resonant states of HC_6H (upper left), HC_8H (upper right), HC_{10}H (lower left), and HC_{12}H (lower right). The negative and positive lobes of these π^* resonances are shown with different colors.

(A color version of this figure is available in the online journal.)

increasing lifetimes as the chain lengthens. In other words, all the larger polyynes show the presence of narrow near-threshold resonances that come further down in energy or become bound states as the chain acquires more carbon atoms.

The spatial features of the lowest resonant wave functions of the scattered electron in the continuum are shown schematically in the four panels of Figure 7, where the real part of the scattering

wave functions are shown over the nuclear locations of the molecular equilibrium geometries.

The data in Figure 7 clearly show the alternative nature of the resonant states, which tend to avoid the molecular regions where triple bonds exist. Furthermore, one clearly sees that all the terminal H atoms acquire no extra electron density as the metastable anion is formed, hence indicating that possible DEA mechanisms leading to de-hydrogenation will very likely form the C_nH^- anionic moiety plus an H atom. Thus, in the case of efficient dynamical couplings between the resonant electron's excess energy and the molecular modes of vibration, one can expect the local excitation of the C–H stretch modes. These stretch modes, in their asymmetric form, will further induce a dipole moment in the system. The quantum structure calculations of Section 2 have indeed shown that such stretching modes will induce a strong dipole moment in the deformed systems and the present scattering calculations additionally suggest that such C–H deformation modes could occur in the polyynes after metastable anions are first formed close to the threshold. In other words, the extra-electron excess energy could be causing such bond deformations involving the terminal H atoms and then could evolve as near-threshold DSSs that can finally recombine with the H^+ region of the deformed molecule (see again Figures 1–4), thereby leaving a stable C_nH^- residual anion, as experimentally observed.

In the following subsection, we will further show that polar polyynes indeed present a new feature in electron scattering processes: the appearance of DSSs, as already discussed in Section 2.

4.2. Threshold Scattering States for Polar Targets

We have briefly discussed in Section 2 the special effects that electron interactions with polar molecules exhibit as a function of the dipole's strength (Fermi & Teller 1947; Garret 1982). We have also discussed that a critical value of the dipole exists for which the target has at least one bound state close to threshold: a DBS state. In the same vein, we will show in the following discussion that the same systems can exhibit dipolar states in the continuum near the positive energy threshold and that such states acquire the spatial structures associated below threshold with the DBS configurations of bound anions: strongly localized outside the molecular volume at the positive side of the dipole's orientation, with a visible nodal plane associated with the p character ($\ell = 1$) of the DSS configurations.

We have carried out such calculations for the radical polar species first, i.e., for the C_4H , C_6H , and C_8H open shell (doublet) systems. The electron scattering from such targets is known to lead to two different scattering cross sections: the singlet cross section σ_s and the triplet cross section σ_t (Curik et al. 2001):

$$\sigma_{\text{tot}} = \frac{1}{4}\sigma_s + \frac{3}{4}\sigma_t. \quad (10)$$

However, given the chief interest of this study in the location of specific threshold states largely independent on the total spin of scattering partners, we have opted to produce scattering observables for average configurations where the target densities of the radicals are independent of their total spin (see also Curik et al. 2001).

Given that the polar long-range interaction is proportional to R^{-2} , the inner box has been increased for the low-energy scattering calculations aimed at locating DSS configurations near-threshold as likely doorway configurations for RS of the

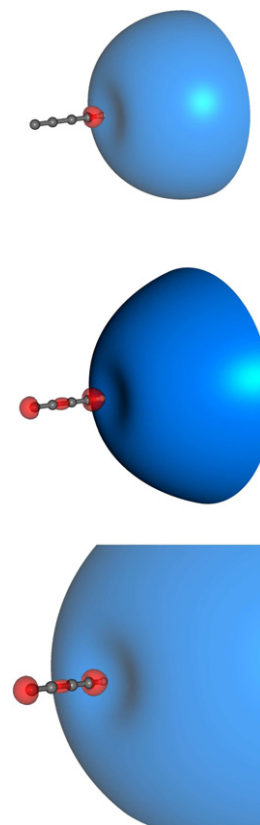


Figure 8. Computed spatial features of the scattering wave functions (real part) for the near-threshold energies of 100 meV (top), 10 meV (middle), and 1 meV (bottom). The target radical molecule is C_4H . The terminal H atom is on the right side of the molecule. See the main text for further details.

(A color version of this figure is available in the online journal.)

threshold-bound states, the DBSs, of the same polar systems. Hence, in the calculations reported, the inner range of the integration box has been extended out to $R_{\text{max}} = 60 \text{ \AA}$, and the numerical tests have been carried out to ensure numerical convergence of the final cross sections. The outer box for the asymptotic matching was extended to 500 \AA to include the dipole potential effects in the near-threshold cross section calculations.

Figures 8–10 show the spatial features of the scattering wave functions (the real part) at collision energies down to 1.0 meV for three exemplary cases of C_nH radicals, with $n = 4, 6$, and 8 .

The following comments can be made looking at the general characteristics of the scattering wave functions reported in these figures.

1. As the collision energies approach the threshold, the scattered electron moves increasingly away from the carbon chain and locates itself outside the H atom, the positive end of the dipole moment.
2. As n increases along the chain and the permanent dipoles become overcritical (i.e., greater than 1.625 D) for $n = 6$ and 8 , the extra electron gets distributed around the H-end of the molecules but also envelops the carbon chains: these are dipole states in the continuum that increasingly resemble the DBS on the negative energy scale found in previous studies (e.g., Simons 2008) to surround the polar targets exactly in the same manner. We will provide below further evidence for the existence of such special states in the bound anionic radicals.
3. The fact that C_4H has a value below the critical dipole strength threshold (Table 1) also shows up in the present

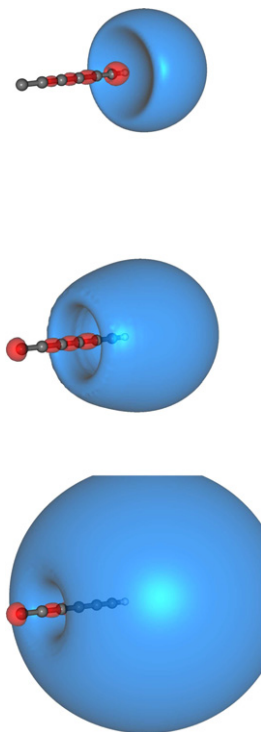


Figure 9. Same as in Figure 8 but for the C_6H polyynyl radical. (A color version of this figure is available in the online journal.)

calculation by the presence of DSS configurations totally outside the polar molecules. These molecules are hence less likely to decay into bound anions by coupling radiatively with the molecular modes, with which little overlap exists (see the DBS calculations below). Furthermore, and as discussed before, the existence in this system of an electronically excited ${}^2\Pi$ state very close to its ground ${}^2\Sigma$ state indicates a large increase in its permanent dipole and therefore the likely formation of a bound DBS (and presumably of a scattering DSS) in the excited electronic state. We shall, however, not pursue this additional avenue in the present study due to its limited importance for the ISM conditions we are discussing here.

4. The radical polyynes with supercritical dipole values, on the other hand, show more clearly that, near the energy threshold, the scattered electron densities in the DSS configurations surround most of the molecule while being located well outside its “molecular” space. Hence, the decay of these radical polymers into DBSs of similar shape at negative energy becomes a likely possibility for chain lengths beyond $n = 4$.

As we have discussed in Section 2, and further described in the preceding subsection on resonant states, the nonpolar carbon chains can also become polar by asymmetric stretching of their C–H bonds. The required energies for such excitations can have different origins, IVR stabilizations of the shape resonances described in the previous subsection being one of the most likely paths. The consequence of such structure deformations leads to polar configurations with supercritical dipole values. Hence, it becomes of interest to see what would be the behavior of such targets in the case of threshold electron scattering events such as those just discussed for their radical counterparts.

Figure 11 shows the spatial features of the scattering wave functions (real part) of asymmetrically deformed nonpolar

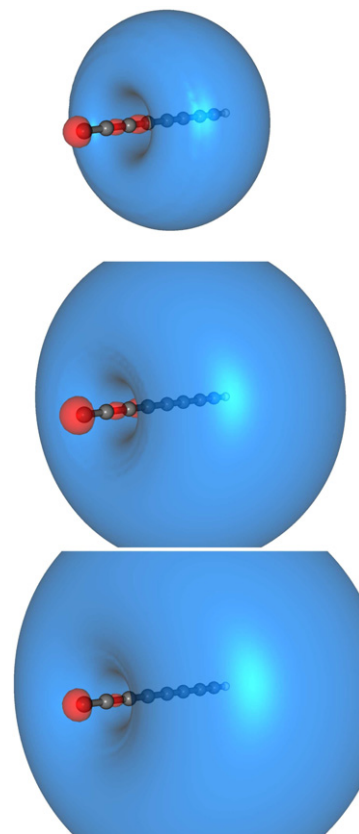


Figure 10. Same as in Figure 8, but for the radical polyynyl molecule C_8H . See the main text for further details.

(A color version of this figure is available in the online journal.)

chains at the near-threshold energy of 1 meV. The figure also shows the stretching of one of the C–H bonds that bring their dipole values beyond the critical values, as shown in Figures 1–3.

The scattering wave functions now show very similar shapes and features as those discussed for the radical species in Figures 8–10: the H atom of the stretched bond now constitutes the positive end of the dipole and the scattered electron becomes localized exclusively outside that atom, thus creating an excess charge distribution over that region of the molecular geometries. If we further consider that the likely stretching path of these polyynes would, according to the calculations discussed in Section 2, preferentially follow the ionic bond break-up, i.e., by forming a sort of $H^+ - C_nH^-$ complex, then it stands to reason to suggest that the scattering of threshold electrons by such distorted species would eventually lead to neutralizing recombination and bond break-up, thereby producing $H + C_nH^-$ species. The latter would initially be the bound DBS configurations, which would be efficiently reached given the small energy gap between them and the DSSs.

One can further verify the extended spatial distribution of the scattered electron by plotting the lower partial waves that contribute to the radial shape of the scattering wave functions. The data in Figures 12 and 13 show such radial extension for the distorted, closed-shell polyynyl configurations just examined above.

Both Figures 12 and 13 clearly show that the scattered electrons reside essentially outside the region of the carbon chains and, as the chain length increases from top to bottom, its radial components become non-negligible at increasingly larger radial values. The scattered electron is in the DSS configuration

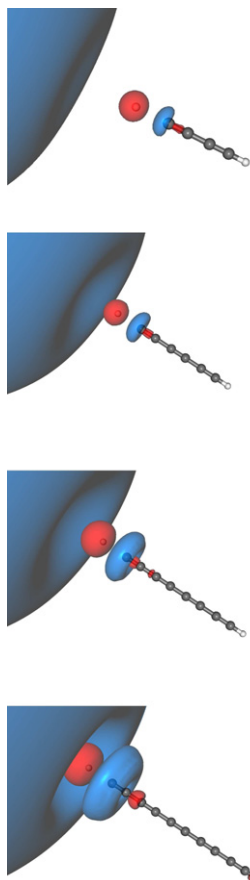


Figure 11. Computed scattering wave functions (real part), for asymmetrically deformed nonpolar chains. The chain length increases from top (HC₄—H) to bottom (HC₁₀—H). The stretched H atom is on the left end of each molecule. See the main text for further details.

(A color version of this figure is available in the online journal.)

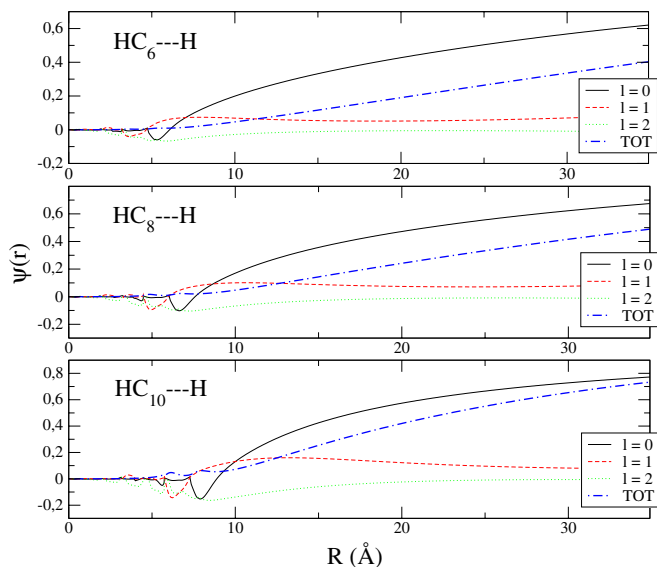


Figure 12. Computed radial components of the scattering wave functions for $\ell = 0, 1,$ and 2 and total radial functions (TOT) over a range of 30 \AA , for the distorted target configurations of Figure 11 with $n = 6, 8,$ and 10 . See the main text for discussion. The collision energy is 1 meV .

(A color version of this figure is available in the online journal.)

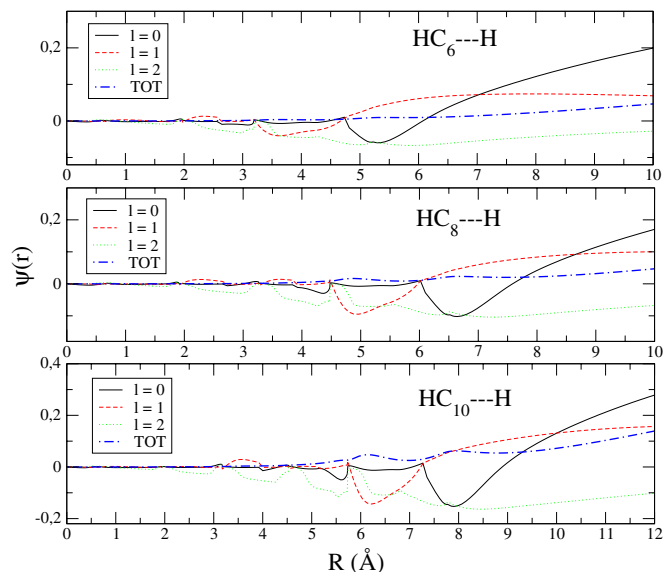


Figure 13. Same as in Figure 12, but for the range up to 10 \AA ($n = 6, 8$) and up to 12 \AA ($n = 10$).

(A color version of this figure is available in the online journal.)

discussed before and localizes in the region of the stretched H atom. This result means that the suggested stabilization path outlined in Sections 2 and 4, namely



is also surmised by the present calculations.

In conclusion, we have shown that both the polar radicals C_nH and the closed-shell HC_nH species with deformed, stretched configurations can exhibit near-threshold scattering states with special features due to the dominant dipole–charge interactions: the DSSs. It now remains to link such states with the near-threshold bound states of the anions: the DBSs discussed before. This work will be done in the following subsection using structural calculations.

4.3. Dipolar-bound States of Radicals

In the previous subsections, we have seen how the low-energy scattering states of electrons interacting with polar radicals polyynes, when their dipole values are close or above the critical value, reveal the occurrence of special spatial shapes of the continuum electrons close to the energy threshold (e.g., in the range of a few meV of the collision energy). Such scattering states were seen to localize chiefly on the H-end of the carbon-rich chains of radical species and to exhibit one nodal plane between the external region and the chains of carbon atoms.

We have called those states DSSs in order to underline the main component of the electron–molecule long-range interaction that contributes to the creation of such states. We also noted that in the case of C_4H^- , where the dipole moment is subcritical, these states are less extreme in terms of spatial location.

We have already noted that the same radical molecules exhibit very large (and positive) EAs (Table 1). Since these molecules have very large dipole moments for $n > 4$, it should be possible that they also support electronically excited anionic states with very small EAs that are caused by the attachment of the extra electron into a Rydberg-like state that presents at least one nodal plane (a p -type dipolar state) and also resides well outside the molecular volume.

Table 3
Computed Vertical Electron Affinity (VEA) for Some of the Radical Polyynes Associated with DBS Formation

	ϵ_{SOMO}	SCF	MP2	CISD
HC ₄	+0.54	-0.67	-0.65	-0.65
HC ₆	-8.43	+7.00	+23.65	+14.19
HC ₈	-7.07	+5.91	+20.15	+11.35
HC ₁₀	-7.62	+6.10	+28.22	+13.22
HC ₁₂	-5.99	+4.93	+20.15	+9.51

Notes. All the values reported are in meV. See the text for further details and an explanation of the values in the columns.

The first column in Table 3 reports the eigenvalues of the higher SOMOs (singly occupied MOs) for the anionic radical species calculated at the SCF level with a basis set expansion given by cc-pVTZ with extended even-tempered (sp)-functions with GTO exponents given by the following formula:

$$2 \times 10^{-5} \times (3.2)^{N-1},$$

with $N = 1-8$. One clearly sees there that even at that single determinant level, the extra electrons associated with triplet states lying closer to the energy threshold exhibit negative eigenvalues for carbon chains with $n > 4$ and therefore indicate positive vertical electron affinities (VEAs) for the larger terms of the series. The next three columns in Table 3 report the actual calculations for the VEAs (essentially coinciding with the adiabatic EAs since the anions here preserve the geometry of the neutral counterparts) at an increased level of treatment of correlation effects. Here, again one sees that increasing the correlation contributions reduces the VEAs because of the stronger attraction of the Rydberg-like extra electron by the remaining bound electrons, but the values still remain all positive and small: the signature of an excited electronic state of the polyyne anion associated with the formation of a DBS.

Even more revealing are the corresponding density maps of the extra electrons shown in Figure 14. One clearly sees that the C₄H molecule is again a special case in which the sub-critical value of its dipole does not allow for the presence of an excited state with a dominant density outside the molecular volume. On the other hand, all the longer C_nH chains exhibit spatial distributions that are similar to those created by the scattering calculations in the same systems and reported in the previous figures.

The dipole-driven states at energies very close to the energy threshold (both in its positive and its negative branch) therefore show very similar spatial behaviors and both localize outside the molecular chain on the H-end of the molecules, becoming increasingly larger as n increases. One can therefore expect that the DBS anionic states could be efficiently reached by RS of the near-threshold scattering states discussed before. Since both states acquire very similar spatial shapes, they would have very strong overlap in the spatial regions outside the linear chain of carbon atoms.

It now remains to discuss how such a variety of processes following electron scattering at low energies could be morphed into providing a realistic modeling of the final attachment rates. In other words, the calculations that we have described in Sections 2 and 4 indicate that resonant compounds and dipolar states, either in the scattering continuum or as bound states (DSSs and DBSs, respectively) could exist for polar carbon-rich chains and that their RS paths could be competitive paths with respect to AD electron losses. Such possibilities could then

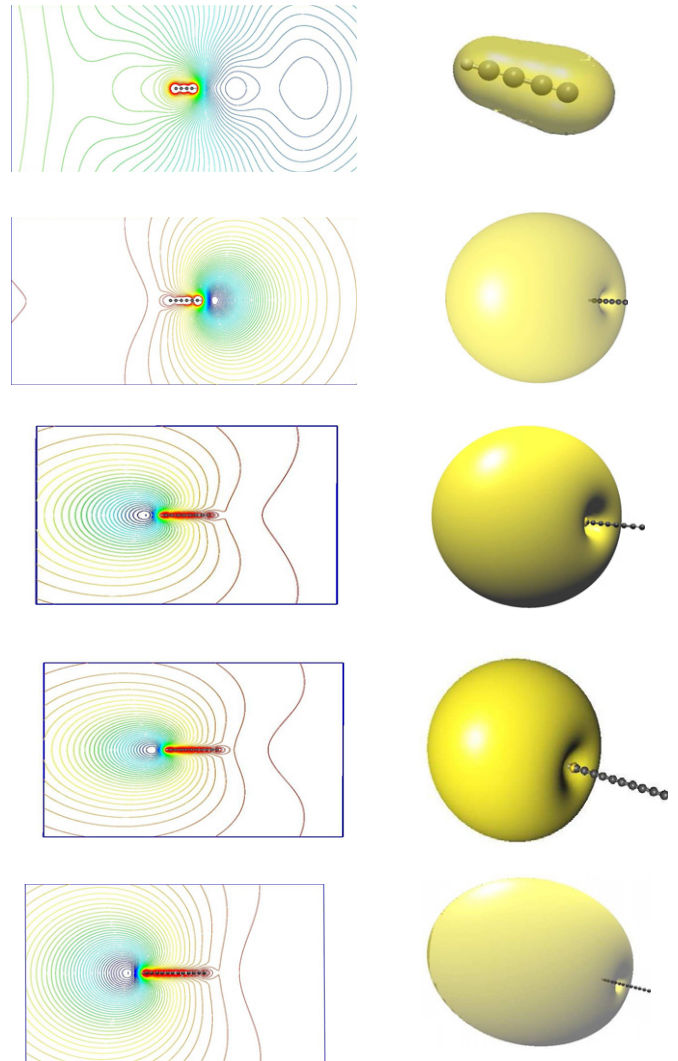


Figure 14. Computed density maps (energy levels on the left and spatial distributions on the right) for the excited DBSs of C-chain anions, from $n = 4$ up to $n = 12$. The terminal H atom is on the left in each molecule. See the text for further details.

(A color version of this figure is available in the online journal.)

provide an approximate way for linking their cross sections with the electron attachment rates needed in the evolutionary modelings.

5. MODELING ATTACHMENT RATES

The previous analysis of such a variety of processes relates to the possible shapes and sizes of the scattering cross sections over the complete range of regions with lower energy. Such dynamical analyses have also revealed before the presence of resonances for metastable electron attachment (Sebastianelli & Gianturco 2012) that indicate the important formation of transient negative ions (TNIs). Such cross sections can therefore give the corresponding rates as:

$$k_{\text{EA}} \simeq k_{\text{TNI}} \quad (12)$$

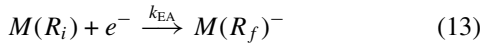
$$k_{\text{TNI}} = \frac{\sqrt{\frac{8K_B T_e}{\pi \mu_e}}}{(K_B T_e)^2} \int E \sigma_0(E) e^{-E/K_B T_e} dE.$$

In our present model, the above rate coefficient is obtained by a convolution over electron temperatures (T_e) of the integral,

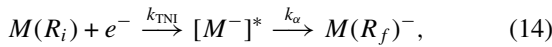
total cross sections $\sigma_0(E)$ that comprise all metastable attachment processes over the mentioned energy range, including the sum over elastic and rotational excitation processes starting with the $|j\rangle = 0$ states of the targets. To model the interstellar environment in our calculation of the cross sections (e.g., see Lucchese & Gianturco 1996 for details), the channels associated with electronic and vibrational excitations are not included; in any case, the whole quantum dynamics of the scattering of electrons from polyynes has been computed considering ab initio methods—see Section 3. Furthermore, from previous analysis of polyatomic targets, we know that the inelastic cross sections at the relevant energies account for approximately 10% of the integral cross sections and hence they would not affect much the values of σ_0 in Equation (12) (Irrera & Gianturco 2005).

It is worth noting that the σ_0 cross sections are calculated by using fixed nuclei geometries of the target polyynes, and therefore the needed dynamical couplings of the nuclei with the electron motion, necessary to retrieve the DEA cross sections, are not present. However, the geometries take into account accurate evaluations from first principles of all the resonance formation states and include the virtual state effects. Thus, within the reduced FN scheme, that excludes vibration for the moment, the found rates would be upper bounds on the EA rates, since all integral cross sections are considered to lead to stabilization of the anion.

The complete electron-attachment process



can be divided into a first attachment stage (labeled as k_{TNI}) and a subsequent process (k_α) that, via IVR, will give a stable anion as described by the following prototypical reaction:

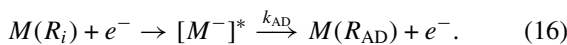


where M stands for the undissociated neutral molecular target and R_i (R_f) refers to the initial (final) molecular geometry. In the above equation, k_α can be obtained by following different stabilization paths, between which the processes mentioned earlier in Sections 4.2 and 4.3 play a role because they could actually contribute to the formation of a DBS of both the polar radical and the neutral distorted polyynes.

On the other hand, another possibility is indeed represented by the RS:



as well as by the DA, where the dehydrogenation process discussed before could also occur. Note that both possibilities are in competition with the AD process



We indicate likely changes in the molecular geometry by R_{DBS} and R_{AD} or, more generally, by R_f depending on the occurrence of the RS, the AD, and also the stabilization by internal excitations involving nuclear geometry deformations (thus including both the DEA and DBSs formation via low-energy DSSs, as discussed before). We also emphasize that all the scattering calculations in the present work were performed in the equilibrium geometry, so that R_i implicitly refers to the minimum energy nuclear configuration for the neutral molecular target.

All the above processes were assumed to occur via either resonance states, where the TNIs played the role of gateway states to the final formation of all stable anions, or via the dipolar states in the continuum formed by scattering from polar targets. In the present cases, those targets will be either the radical species or the distorted closed-shell species that also lead to anionic radicals. Thus, the calculations included in this work generate from first principles all the states that are expected to contribute to the anion formation rate, including all the zero-energy resonances and virtual states that can occur when the energy of the collision tends to zero and that can still contribute to k_{EA} .

It is worth noting that the final rate of electron attachment, k_{EA} , can be associated to the rate that controls the formation of the metastable anion (k_{TNI}) and to the AD and RS rates, namely k_{AD} and k_{RS} (Carelli et al. 2013):

$$k_{\text{EA}} = \left(\frac{k_{\text{RS}}}{k_{\text{AD}} + k_{\text{RS}}} \right) k_{\text{TNI}}, \quad (17)$$

when anionic formation is assumed to be in a steady state (Herbst 1981). Since it is also assumed that k_{AD} and k_{RS} are strictly positive, one can further write:

$$k_{\text{EA}} < k_{\text{TNI}}, \quad (18)$$

which suggests that the quantities we seek to evaluate, the electron attachment rates k_{EA} , have a clear upper bound in the rates we calculate by including all resonant and dipolar processes within the (elastic+rotational) integral cross sections: the k_{TNI} rates. On the other hand, previous studies of attachment rates (e.g., Harada & Herbst 2008) have shown that the inclusion of vibrational channels increases the phase-space region to be considered and includes channels with much larger Einstein coefficients. Hence, vibrational channels may still play an important role in estimating the final attachment rates. The fact that we are at the moment not including vibrational attachment channels, however, means that our rates make an artificial reduction of the available phase-space size and therefore could still turn out to be of the correct size by generating larger rates but in a reduced phase-space domain. Hence, the present calculations, besides suggesting specific mechanisms that are likely to preside at the formation of final stable anions of radical polyynes (the C_nH^- species also experimentally observed, e.g., Cernicharo et al. 2007), can also provide realistic cross sections from which we can generate fairly realistic values for the electron attachment rates. Although, in fact, we assume that all the elastic cross sections are taken to lead to attachment, such cross sections are still not including the contributions of vibrational channels and hence may turn out to be the correct size through cancellations of errors with opposite signs.

Figure 15 shows three examples of k_{EA} rates associated with C_4H^- (top), C_6H^- (middle), and C_8H^- (bottom) from near-threshold temperature up to about 10^3 K. It is interesting to note that the order of magnitude of our rates is around $10^{-8} \text{ cm}^3 \text{ s}^{-1}$, which is not very different from values suggested earlier (Herbst & Osamura 2009) for the whole class of polyynes.

Given that the dipole–charge interaction dominates near-threshold, we furthermore see in Figure 15 how all the calculated rates increase as the temperature decreases. On the other hand, the results reported by Figure 16, and dealing with the closed-shell, nonpolar polyynes, appear to tell a different story.

We see, in fact, that the lack of a permanent dipole moment in the molecular partners strongly reduces the rates of electron

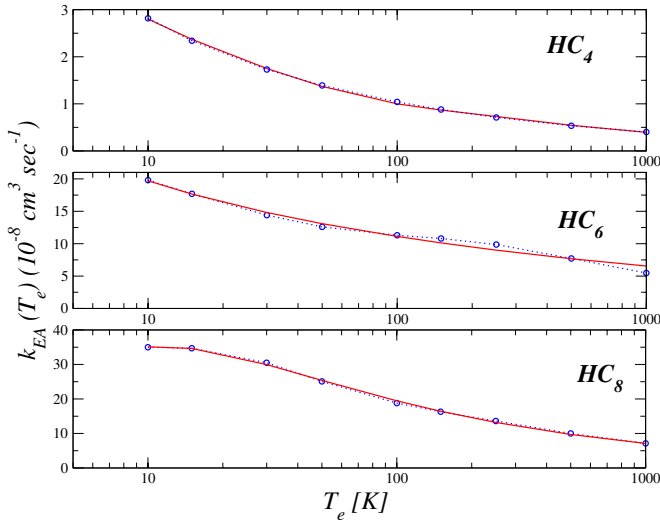


Figure 15. Computed electron attachment rates (circles), k_{TNI} , as a function of electronic temperature T_e , for three different examples of radical polyynes. The solid lines were obtained by fitting the previous values by using a specific parametric expression (as reported in Equation (19)). See the main text for further details.

(A color version of this figure is available in the online journal.)

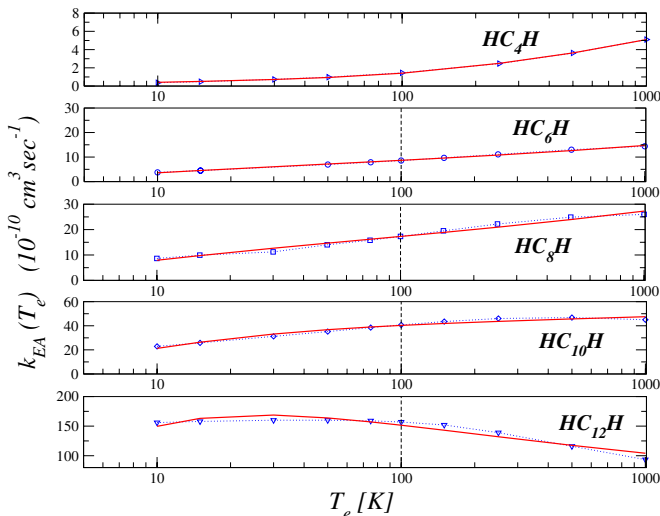


Figure 16. Computed electron attachment rates as those in Figure 15, but for the closed-shell nonpolar polyynes of the present work. See the main text for further details.

(A color version of this figure is available in the online journal.)

attachment for all the terms of the series: they are all of the order of $10^{-10} \text{ cm}^3 \text{ s}^{-1}$, i.e., around 100 times smaller than those of radical species with the same carbon-chain lengths (Figure 15). This fact explains why the current observations do not report the presence of HC_nH^- members in the anionic polyne series since their permanence in sufficient concentration would be strongly reduced by the reduced efficiency of anionic formation and the possible prevalence of either AD channels or the DEA dehydrogenation channels discussed in the previous sections: the net outcome would be in both cases the disappearance of HC_nH^- species. On the other hand, the radical polar partners are seen to yield much higher values for the computed k_{EA} values over the whole range of relevant temperatures: the suggested mechanisms of the present work clearly favor C_nH^- formation over HC_nH^- formation, as is indeed indicated by experiments.

Table 4
Fitting Coefficients for the Polyne Electron Attachment Rates, k_{2B}

	α	β	γ
HC ₄	0.66(−8)	−0.410	0.56
HC ₆	8.62(−8)	−0.227	0.53
HC ₈	12.39(−8)	−0.457	5.16
HC ₁₀	21.24(−8)	−0.295	0.00
HC ₁₂	28.08(−8)	−0.295	0.00
HC ₄ H	2.74(−10)	0.525	2.93
HC ₆ H	11.45(−10)	0.212	4.38
HC ₈ H	21.99(−10)	0.182	4.02
HC ₁₀ H	45.07(−10)	0.049	5.86
HC ₁₂ H	130.25(−10)	−0.181	4.78

Notes. α is given in $\text{cm}^3 \text{ s}^{-1}$, β is dimensionless, and γ is in K. Note that $A(-B) = A \times 10^B$.

In current evolutionary models of chemical networks, the general two-body (2B) reactions like the ones we are discussing here are usually represented by a commonly used parametric form (Carelli et al. 2013):

$$k_{\text{EA}} = k_{2B} = \alpha \left(\frac{T}{300 \text{ K}} \right)^\beta \exp\left(-\frac{\gamma}{T}\right) \text{ cm}^3 \text{ s}^{-1}. \quad (19)$$

We have employed such a form for the fitting of the radical anion and nonpolar polyynes anion formation rates; the quality of the fitting can be seen from the additional curves present in both Figures 15 and 16, while the actual values of the coefficients are given in Table 4. The parametric values used for the full series were obtained by combining the calculated ones for $n = 4, 6,$ and 8 with the interpolated values for $n = 10$ and 12 .

6. EFFECTS OF THE PRESENT RATES ON ISM EVOLUTIONARY CALCULATIONS

In order to verify the effects of the ISM on the new calculations, we have developed a one-zone time-dependent model (e.g., see Wakelam & Herbst 2008; Walsh et al. 2009, or Carelli et al. 2013) representing a dark cloud core. It evolves from a given set of initial abundances at constant temperature, density, cosmic-ray flux, and gas UV opacity. We follow the reaction rates and the species found in The Ohio State University chemical network labeled `osu_01_2009`⁴ (OSU); the data include anions as C_nH^- ($n = 4, 6, 8,$ and 10) that are involved in mutual neutralization reactions ($\text{A}^+ + \text{B}^- \rightarrow \text{A} + \text{B}$), photo-detachment ($\text{A}^- + h\nu \rightarrow \text{A} + e^-$), associative detachment ($\text{A}^- + \text{B} \rightarrow \text{AB} + e^-$), anion-neutral reactions ($\text{A}^+ + \text{B}^- \rightarrow \text{C} + \text{D}^-$), and electron attachment ($\text{A} + e^- \rightarrow \text{A}^- + h\nu$). The total number of species is 469, while number of reactions is 6045.

In our calculations, we employed the DLSODES solver (Hindmarsh 1983) with a relative and absolute tolerance of 10^{-10} and 10^{-40} , respectively, which allows for reliable numerical stability.

The initial abundances for the different species reported in Table 5 are the same as in Graedel et al. (1982); these abundances correspond to an oxygen-rich and a low-metallicity environment. The values listed refer to the fractional abundances with respect to the atomic hydrogen total density (in our case, $n_{\text{H}} = 10^4 \text{ cm}^{-3}$), while, to guarantee the global cloud neutrality, the number density of free electrons is $n_{e^-} = \sum_i n_i$, where the

⁴ http://physics.ohio-state.edu/~eric/research_files/osu_01_2009

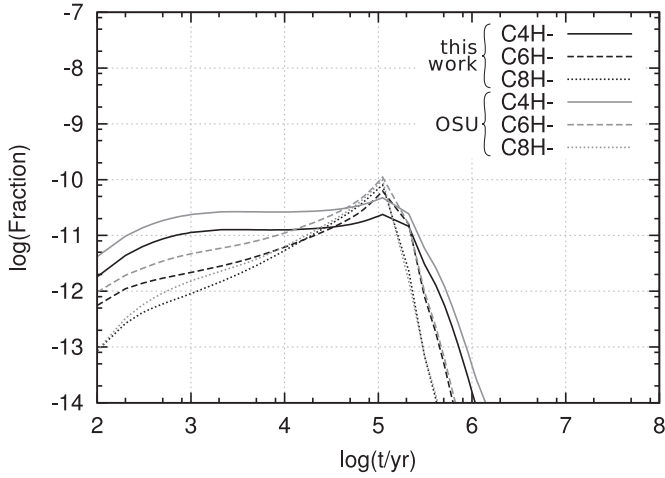


Figure 17. Evolution with time of C_4H^- (solid), C_6H^- (dashed), and C_8H^- (dotted), using the electron attachment coefficients from the OSU database (gray) and the rate calculated in this work (black).

sum runs over the positive ions. The other parameters employed for our calculations are the temperature of the gas $T_{\text{gas}} = 10$ K, the visual extinction $A_V = 10$ mag, the cosmic-rays ionization rate $\zeta = 1.3 \times 10^{-17} \text{ s}^{-1}$, and a dust to gas ratio of zero (i.e., a dust-free model).

We have run two models for 10^8 yr: the first with the original OSU database, while the second with their electron attachment rates replaced by the coefficients computed in our present work. In both models, the abundance of the anions grows in the first 10^5 yr when their formation is controlled by the electron attachment rate, and then it starts to decrease rapidly as the number of neutral precursor C_nH decreases (see the left panel of Figure 18). At the same time, other competitive reactions start to prevail; including the associative detachment involving H and O atoms and therefore the various mutual neutralization with the ions that populate the ISM in this stage of the evolution. As expected, the effects of the new rates on the C_nH^- evolution (Figure 17, black lines) are smaller than those from the rates obtained in the previous section, obtained using the values found in the OSU chemical network (gray lines). From the plots, we also note that the efficiency in forming the C_nH^- species is slightly higher in the OSU model, since at $T_{\text{gas}} = 10$ K

Table 5
Initial Abundances with Respect to the Total Atomic Hydrogen (Graedel et al. 1982)

Species	Fractional Abundance
H_2	5.00(-1)
He	1.40(-1)
C	7.30(-5)
N	2.14(-5)
O	1.76(-1)
S^+	2.00(-8)
Si^+	3.00(-9)
Na^+	3.00(-9)
Mg^+	3.00(-9)
Fe^+	3.00(-9)
P^+	3.00(-9)
F	2.00(-8)
Cl	3.00(-9)
e^-	See the text

their rate coefficients are more effective at forming anions than what is suggested by our calculations. The global charge of the dark cloud, i.e., $\sum_i n_i$ (where the sum runs over all the anions and free electrons), is almost not affected by the rates presented in this work, as shown in the right panel of Figure 18. The left panel of the same figure reports the behavior of the neutral species evolutions due to various fragmentation reaction processes. Their evolution indicates that efficient neutralization rates initially increase neutral formation while the efficient attachment rates reduce free electrons later in the evolution, together with the chemical destruction of neutral chains.

However, the general trend is certainly similar in both calculations: in spite of the very different physical mechanisms suggested by our present study with respect to earlier analyses (Herbst & Osamura 2009), the above findings indicate that we have now a sort of confirmation of the expected efficiency of the electron attachment role during the dark cloud evolutionary models.

7. PRESENT CONCLUSIONS

The work that we have reported in the present paper attempts to provide computational evidence for several aspects of the

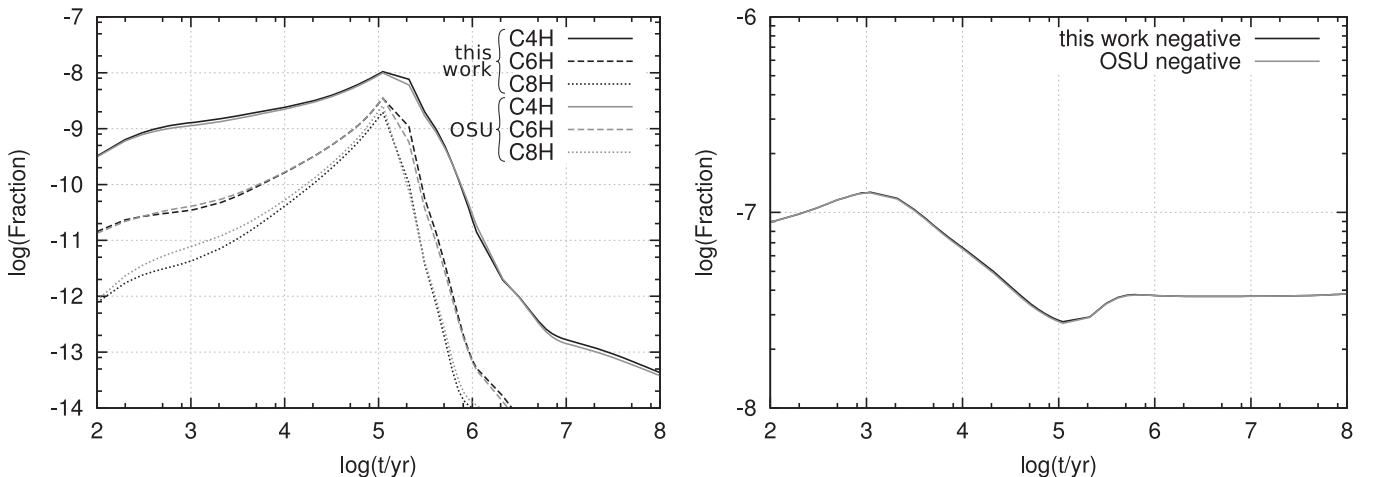


Figure 18. Left: evolution with time of C_4H (solid), C_6H (dashed), and C_8H (dotted) using the electron attachment coefficients from the OSU database (gray) and the rate calculated in this work (black). Right: evolution of the sum of the negative species and electrons (see the text). Note that the two lines from the two different models nearly overlap.

physics of the formation of negative ions of carbon-rich linear chains in the ISM.

1. The molecular mechanism for low-energy direct electron attachment to radical chains of the C_nH type, with n related to the species most observed in the ISM experiments: C_4H , C_6H , and C_8H .
2. The likely molecular mechanism for the fragmentation-after-attachment to nonpolar closed-shell polyynes of the HC_nH type via intermediate metastable anions of the $[(HC_nH)^-]^*$ type, leading to the disappearance of direct $(HC_nH)^*$ anion formations.
3. The ensuing energy dependence of the total cross sections for both systems, from threshold to the higher energies required to yield the corresponding rates over a broad range of electron temperatures.
4. The employment of the electron-attachment rates computed for the C_nH^- systems within a one-dimensional model of the chemical network's role associated with dark cloud evolutionary conditions.
5. Comparison of the present findings with the earlier results of similar evolutionary calculations.

The calculations of the present study suggest a specific low-energy mechanism for electron-attachment processes that makes it very competitive with the AD channels that could inevitably deplete anionic formation. Due to the supercritical permanent dipole values in the larger members of the series ($n > 4$), we find the existence of dipole-driven states of the radical polyynes both at near-threshold energy in the continuum (the DSSs discussed earlier) and as excited bound anionic states with attachment energies of a few meV (the DBSSs discussed earlier). The presence of dipole-driven states during the scattering process with the low-energy electrons of the ISM would allow for efficient RS paths involving states that are very close to each other in shape and size and that would thus require negligible contributions from the slower nuclear rearrangement effects during the stabilization time. Furthermore, the very small energy gaps existing between the initial DSSs and the final discrete DBSSs for the present systems will also operate toward a more efficient formation of bound anions in competition with the AD channels.

Our study has also investigated the possible role of similar polyynes of the nonpolar (HC_nH) series that could undergo electron attachment under the same electron density of the ISM environment of their radical counterparts. Our calculations have found that such systems have low-energy resonances, with energies of about 1 eV or less, which could lead to energy transfer into the asymmetric stretching mode by IVR processes. Such deformed states of the closed-shell polyynes are shown to acquire very large dipole moments whereby the initial resonant electrons become near-threshold DSSs after the IVR energy losses. Furthermore, the deformed molecules are observed to undergo ionic bond-stretching as the more efficient paths and therefore find the cationic end of the chain surrounded by the scattering electron density, thereby leading to recombination processes of the type $H^+ + e^- \rightarrow H$ that leave the residual radical with negative charge. These processes favor the final formation of anionic triplet states of the C_nH^- type, as was the case for the previous group of polyynes. In other words, the possible presence of both HC_nH and C_nH molecular species in the ISM would preferentially lead to C_nH^- anionic formation when interacting with low-energy free electrons in that environment, thus confirming the observation of the latter anions and not the

former ones. The computed electron attachment rates, albeit originating from a modeling based on the elastic total cross sections as described in one of the previous sections, also show very marked differences in values between those of the radical species and the smaller ones for the nonpolar, closed-shell molecules. Hence, it becomes reasonable to suggest that the latter anionic molecules will be less efficiently formed and therefore will be more difficult to observe. On the other hand, the rates for electron attachment that we obtain in the present study indicate, once included in a chemical network evolutionary modeling as described in the previous section, that the final presence of anionic polyynes that our calculations predict (and the corresponding disappearance of the electrons of the environment) are very close to those indicated in earlier studies (Walsh et al. 2009), although these earlier studies suggest a different model for the mechanism of electron attachment. Thus, the present size and range of the attachment rates is suggested by at least two different models for their molecular mechanism of formation, although in the present analysis we carry out the calculations at a more detailed level than before and explicitly include the quantum dynamics of the attachment process from actual scattering calculations.

It is also interesting to mention at this point that the chemical attachment processes described in the present work belong to the broader class of chemical reactions driven by dipolar and polarization forces, i.e., that these processes belong to the very extensive domain of ion-molecule reactions in the ISM that have been studied and analyzed in many different contexts (e.g., Bohme 1992).

The financial supports of the PRIN 2009 national research network, of the "Chemical Cosmos" COST network, and of the CINECA Supercomputing Consortium are gratefully acknowledged. T.G. also thanks the CINECA for a Postdoctoral Contract while this work was carried out. F.C. thanks the PRIN 2009 network for a postdoctoral fellowship.

REFERENCES

- Allan, M., May, O., & Fedor, J. C. I. B. 2011, *PhRvA*, **83**, 052701
- Baccarelli, I., Sebastianelli, F., Nestmann, B., & Gianturco, F. A. 2013, *EPJD*, **67**, 93
- Bohme, D. K. 1992, *Chem. Rev.*, **92**, 1487
- Brünken, S., Gupta, H., Gottlieb, C. A., McCarthy, M. C., & Thaddeus, P. 2007, *ApJL*, **664**, L43
- Carelli, F., Grassi, T., Sebastianelli, F., & Gianturco, F. A. 2013, *MNRAS*, **428**, 1181
- Carles, S., Desfrancois, C., & Schumann, J. P. 2000, *JChPh*, **112**, 3726
- Cernicharo, J., Guélin, M., Agúndez, M., et al. 2007, *A&A*, **467**, L37
- Cernicharo, J., Guélin, M., Agúndez, M., et al. 2008, *ApJL*, **688**, L83
- Curik, R., Gianturco, F. A., Lucchese, R. R., & Sanna, N. 2001, *JPhB*, **34**, 59
- Dalgarno, A., & McCray, R. A. 1973, *ApJ*, **181**, 95
- Desfrancois, C. 1995, *PhRvA*, **51**, 3667
- Fermi, E., & Teller, E. 1947, *PhRv*, **72**, 399
- Frisch, M.-J. 2009, *Gaussian 03* (Wallingford, CT: Gaussian Inc.)
- Garret, W. R. 1982, *JChPh*, **77**, 3666
- Graedel, T. E., Langer, W. D., & Frerking, M. A. 1982, *ApJS*, **48**, 321
- Graupner, K., Field, T. A., & Saunders, G. 2008, *ApJL*, **685**, L95
- Gupta, H., Brunken, S., Tamassa, F., et al. 2007, *ApJL*, **655**, L57
- Hara, S. J. 1967, *JPSJ*, **710**
- Harada, N., & Herbst, E. 2008, *ApJ*, **685**, 272
- Herbst, E. 1981, *Natur*, **289**, 656
- Herbst, E., & Osamura, Y. 2009, *ApJ*, **679**, 1670
- Hindmarsh, A. C. 1983, *IMACS Trans. Sci. Comput.*, **1**, 55
- Irrera, S., & Gianturco, F. A. 2005, *NJPh*, **7**, 1
- Kawaguchi, K., Kasai, Y., Ishikawa, S., & Kaifu, N. 1995, *PASJ*, **47**, 853
- Lucchese, R. R., & Gianturco, F. A. 1996, *IRPC*, **15**, 429
- McCarthy, M. C., Gottlieb, C. A., Gupta, H., & Thaddeus, P. 2006, *ApJL*, **652**, L141

- McCarthy, M. C., Gottlieb, C. A., Thaddeus, P., Horn, M., & Botschwina, P. 1995, *JChPh*, **103**, 7820
- Perdew, J. P., & Zunger, A. 1981, *PhRvB*, **23**, 5048
- Remijan, A., Hollis, J. M., Cardiner, M. A., et al. 2007, *ApJL*, **664**, L43
- Sarre, P. J. 1980, *JCPPC*, **77**, 769
- Sebastianelli, F., Carelli, F., & Gianturco, F. 2012, *CP*, **398**, 199
- Sebastianelli, F., & Gianturco, F. A. 2010, *EPJD*, **59**, 389
- Sebastianelli, F., & Gianturco, F. A. 2012, *EPJD*, **66**, 41
- Simons, J. 2008, *JPCA*, **112**, 6401
- Taylor, J. R. 1972, *Scattering Theory* (New York: Wiley)
- Thaddeus, P., Gottlieb, C. A., Gupta, H., Brunken, S., & McCarthy, M. C. 2008, *ApJ*, **677**, 1132
- Wakelam, V., & Herbst, E. 2008, *ApJ*, **680**, 371
- Walsh, C., Harada, N., Herbst, E., & Millar, T. J. 2009, *ApJ*, **700**, 752